Journal of
Electrical and Electronic Materials

View Online CrossMark
Regular Paper

Manufacturing Process Optimization of Oxide-Based Multilayer Ceramic Batteries Using Multilayer Ceramic Processing Technologies

Won-Su Lee, Jong Kyu Lee, Jung Rag Yoon*

R & D Center, Samwha Capacitor, Yongin 17118, Korea

Corresponding author(s): yoonjungrag@samwha.com (J.R. Yoon)

Cite as J. Electr. Electron. Mater., 39(5), 519–531 (2026), DOI: https://doi.org/10.4313/JEEM.2026.39.5.9

Received June 24, 2026; Revised July 13, 2026; Accepted July 13, 2026

ABSTRACT: Multilayer ceramic batteries (MLCBs) have attracted increasing attention as compact all-solid-state energy-storage devices that can be manufactured using multilayer ceramic processing technologies. In this study, an MLCC-compatible fabrication process for oxide-based MLCBs was developed using $Li_{1+x}Al_xTi_{2-x}(PO_4)_3$ (LATP) solid electrolytes, $Li_3V_2(PO_4)_3$ (LVP) cathodes, and Cu current collectors. Commercial LATP powders were evaluated in terms of particle-size distribution, phase purity, thermal stability, and ionic conductivity. The selected LATP powder was subsequently employed for tape-cast green-sheet fabrication, and the effects of polyvinyl butyral (PVB) binder content on slurry rheology and sheet microstructure were investigated. An optimized binder composition containing 11 wt% PVB (BM-2/BH-3 = 3:7) provided improved processability and microstructural uniformity. Drying conditions during sequential electrode printing were also optimized to suppress sheet warpage and improve multilayer registration. Thermogravimetric and differential thermal analyses (TG–DTA) were used to establish an optimized two-step debinding and co-firing process under a controlled reducing atmosphere. The resulting multilayer structures exhibited uniform densification without significant blistering, delamination, or interfacial defects. Charge–discharge measurements confirmed that electrochemical functionality was retained after the complete manufacturing process, yielding a discharge capacity of approximately 2.5–2.7 μAh.

KEYWORDS: Multilayer ceramic battery, LATP, LVP, Solid-state battery, Tape casting, Co-firing

1 Introduction

Recent advances in Internet-of-Things (IoT) devices, wireless sensors, wearable electronics, implantable medical systems, and AI-enabled edge computing have created increasing demand for miniature energy-storage devices that can be directly integrated with electronic circuits. Unlike conventional large-format batteries, next-generation micro-energy-storage systems require not only high safety and reliability but also compatibility with surface-mount-device (SMD) assembly and high-volume electronic manufacturing processes. Consequently, considerable research efforts have recently focused on chip-type all-solid-state batteries capable of providing compact form factors, enhanced thermal stability, and improved integration with semiconductor and passive-component technologies. Among the various approaches proposed for miniaturized energy-storage devices, multilayer ceramic batteries have emerged as a promising architecture because they combine the intrinsic safety of oxide-based solid electrolytes with the high volumetric efficiency of multilayer ceramic structures. Similar to multilayer ceramic capacitors (MLCs), MLCBs can be

fabricated using mature multilayer ceramic processing technologies, including tape casting, screen printing, lamination, debinding, and co-firing. Such multilayer architectures shorten lithium-ion transport distances, increase the electrode–electrolyte interfacial area, and enable high-power operation while maintaining compact dimensions. Consequently, MLCBs are increasingly regarded as a promising platform for integrated power sources in next-generation electronic systems. Despite these advantages, several critical challenges remain before practical implementation can be achieved. In particular, successful multilayer battery fabrication requires simultaneous optimization of electrolyte processability, electrode compatibility, shrinkage matching, multilayer registration, interface stability, and co-firing reliability. Therefore, the development of manufacturing technologies capable of integrating electrochemical materials into multilayer ceramic architectures has become a key research topic in the field of oxide-based all-solid-state batteries. Among various oxide-based solid electrolytes investigated for all-solid-state batteries, lithium aluminum titanium phosphate (LATP, $Li_{1+x}Al_xTi_{2-x}(PO_4)_3$) has emerged as one of the most promising candidates because of its NASICON-type crystal structure, high lithium-ion conductivity (~10^{-4}–10^{-3} S cm^{-1} at room temperature), excellent air stability, and compatibility with conventional ceramic processing technologies [1–3]. Unlike sulfide-based solid electrolytes, LATP can be processed under ambient atmospheric conditions and exhibits superior thermal and chemical stability during high-temperature ceramic fabrication. Furthermore, its relatively low sintering temperature compared with garnet-type electrolytes such as $Li_{6.1}Ga_{0.3}La_3Zr_2O_{12}$ (LLZO) makes LATP particularly suitable for multilayer ceramic processing and co-firing applications [2,4]. An additional advantage of LATP is its multifunctional role within oxide-based battery architectures. In addition to serving as a solid electrolyte separator, LATP can also be incorporated into composite cathodes and anodes as a lithium-ion-conducting framework, thereby improving ionic transport across electrode/electrolyte interfaces. Such versatility is highly advantageous for monolithic multilayer ceramic batteries, where minimizing interfacial resistance and maintaining structural integrity are critical requirements. Recent reviews on NASICON-type electrolytes have identified LATP as one of the most practical candidates for scalable oxide-based all-solid-state battery manufacturing owing to its favorable balance among ionic conductivity, process ability, and chemical stability [5–7]. For the active electrode material, lithium vanadium phosphate ($Li_3V_2(PO_4)_3$, LVP) was selected because of its high operating voltage, excellent structural stability, and compatibility with phosphate-based solid electrolytes. LVP possesses a theoretical capacity of approximately 132 mAh g^{-1} and exhibits a stable three-dimensional lithium diffusion pathway with relatively small volume changes during cycling [8,9]. Recent studies have demonstrated that phosphate-based LVP electrodes provide excellent electrochemical reversibility and can be employed not only in conventional lithium-ion batteries but also in symmetric full-cell configurations owing to their structural robustness and favorable redox characteristics [8]. Furthermore, optimization of the sintering atmosphere for LVP has been shown to be essential for its integration into oxide-based all-solid-state batteries, confirming its suitability for ceramic processing routes [10]. The combination of LVP and LATP is particularly attractive for multilayer ceramic battery applications because both materials share phosphate-based crystal frameworks and exhibit favorable chemical compatibility. Their similar thermal stability and ceramic-processing characteristics facilitate co-firing and multilayer fabrication while reducing the risk of severe interfacial degradation. Previous studies have demonstrated the feasibility of integrating phosphate electrolytes and phosphate electrodes into monolithic all-solid-state battery architectures [11]. Therefore, the LVP–LATP system was selected in the present study as a representative oxide-based battery platform for investigating the feasibility of adapting multilayer ceramic processing technologies to scalable MLCB manufacturing. In this work, commercial LATP powders were systematically evaluated through particle-size distribution, phase analysis, thermal characterization, and electrochemical impedance measurements to identify suitable oxide solid electrolytes. LATP green sheets were subsequently optimized through binder-content control, followed by investigations of printing-induced warpage during sequential electrode deposition. A TG–DTA-guided debinding strategy was developed based on the thermal behavior of individual constituents, and its effectiveness in suppressing co-firing defects was experimentally verified. Finally, a functional co-fired multilayer ceramic battery was successfully fabricated, and its electrochemical operation was demonstrated through charge–discharge measurements. The present study establishes a practical manufacturing route toward scalable oxide-based multilayer ceramic batteries using mature multilayer ceramic processing technologies.

2 Experimental Methods

2.1 Selection and Preparation of LATP-Based Green Sheets

Commercial LATP powders supplied by two different vendors were evaluated as oxide solid electrolyte candidates for multilayer ceramic battery (MLCB) fabrication. The powders were characterized in terms of particle size distribution, crystal structure, thermal stability, and ionic transport properties. Particle size distribution was analyzed to evaluate powder uniformity and packing behavior for tape casting. Phase purity was examined by X-ray diffraction (XRD) over a 2θ range of 10–70°, while thermal behavior was investigated using thermo-gravimetric and differential thermal analysis (TG-DTA). Electrochemical impedance spectroscopy (EIS) was performed on sintered LATP pellets and Li/LATP/Li symmetric cells to compare ionic transport characteristics. Based on these results, the LATP powder exhibiting superior phase purity, thermal stability, and lower impedance was selected for subsequent processing. LATP green sheets were fabricated by a tape-casting process. LATP powder was mixed with polyvinyl butyral (PVB) binders (BM-2 and BH-3, Sekisui Chemical Co., Ltd., Japan), dispersant, plasticizer, and organic solvents to prepare ceramic slurries. The PVB binder system consisted of BM-2 and BH-3 mixed at a weight ratio of 3:7. The binder content was varied from 7 to 13 wt% to optimize slurry rheology and green-sheet microstructure. Ethanol and toluene were used as mixed solvents at a weight ratio of 1:1, and the plasticizer content was fixed at 25 wt% of the total binder content. All slurries were ball-milled for 24 h to ensure homogeneous dispersion of the LATP particles. After milling, the slurries were filtered and de-aerated prior to tape casting. The viscosity of each slurry was measured as a function of shear rate to evaluate rheological behavior. The resulting green sheets were characterized by field-emission scanning electron microscopy (FE-SEM) to evaluate particle packing, pore distribution, and microstructural uniformity. Based on the combined rheological and microstructural analyses, the composition containing 11 wt% PVB was selected as the optimized formulation for subsequent multilayer ceramic battery fabrication. For quantitative comparison, the room-temperature ionic conductivity of each sintered LATP pellet was calculated using $\sigma = L/(RA)$, where L is the pellet thickness, R is the total resistance determined from the impedance spectrum, and A is the electrode area. The total resistance was obtained from the intercept of the fitted impedance response with the real axis, including the bulk and grain-boundary contributions. The pellet thicknesses and electrode areas were measured individually before the EIS measurements.

2.2 Multilayer Fabrication and Lamination Process

The optimized LATP green sheets were cut into the desired dimensions and punched with alignment holes for multilayer processing. Lithium vanadium phosphate (LVP, $Li_3V_2(PO_4)_3$)-based paste was employed as the active electrode material, while Cu powder-based paste was used as the current collector. Cathode and current collector layers were sequentially printed using a precision screen-printing process. The printing sequence consisted of cathode printing, current collector printing, and cathode overprinting. After each printing step, the sheets were dried under controlled conditions. Conventional (75/85°C) and optimized (65/75°C) drying profiles were compared to evaluate sheet warpage and electrode registration accuracy. The optimized lower-temperature drying condition was selected because it effectively suppressed thermally induced deformation and improved dimensional stability. The printed sheets were subsequently stacked and consolidated by warm isostatic pressing (WIP) to improve interfacial contact and reduce internal porosity. Layer alignment, dimensional stability, and lamination quality were evaluated using optical microscopy.

2.3 Thermal Processing, Co-Firing, and Electrochemical Characterization

The thermal decomposition behavior of the cathode paste, LATP green sheet, current collector paste, and laminated green chip was analyzed by TG-DTA to establish an optimized debinding process. The major decomposition of organic constituents occurred between approximately 200 and 450°C. Based on these results, a controlled burnout schedule was designed to minimize rapid gas evolution and internal pressure buildup. Following binder removal, the laminated structures were co-fired under a controlled atmosphere to form dense multilayer ceramic batteries. The effects of the burnout process were evaluated through cross-sectional SEM observations, focusing on blister formation, interfacial delamination, pore generation, and layer continuity. The electrochemical performance of the fabricated MLCBs was evaluated by charge–discharge testing. Voltage–capacity profiles were recorded to verify lithium-ion insertion and extraction behavior after co-firing. Stable charge–discharge characteristics without short-circuiting or abnormal voltage collapse were considered evidence of successful fabrication of functional oxide-based multilayer ceramic batteries.

3 Results and Discussion

3.1 Selection of LATP Solid Electrolytes for Multilayer Ceramic Battery Processing

The selection of a suitable oxide solid electrolyte is a critical prerequisite for the successful fabrication of multilayer ceramic batteries (MLCBs), as the characteristics of the starting powder strongly influence slurry stability, green-sheet quality, multilayer registration, densification behavior, and ultimately electrochemical performance. In particular, multilayer ceramic battery processing requires solid electrolytes with high phase purity, narrow particle-size distribution, excellent thermal stability, and low ionic resistance to ensure compatibility with tape casting, screen printing, lamination, and co-firing technologies. Therefore, two commercially available LATP powders supplied by different vendors were systematically evaluated to identify the most suitable material for multilayer ceramic battery fabrication. Figure 1(a) compares the particle-size distributions of the two LATP powders. Vendor A exhibited a relatively broad distribution containing both fine and coarse particles, whereas Vendor B showed a narrower distribution centered within approximately 1–3 μm. Uniform particle-size distribution is advantageous for tape-casting processes because it promotes homogeneous particle packing, improves slurry stability, and facilitates the formation of defect-free green sheets. In contrast, broad particle-size distributions may result in local density variations, differential shrinkage, and structural defects during multilayer processing. The phase purity of the LATP powders was investigated by X-ray diffraction analysis, as shown in Fig. 1(b). Both powders exhibited diffraction peaks corresponding to the NASICON-type LATP structure; however, Vendor B showed higher phase purity without detectable secondary phases. In contrast, weak impurity peaks associated with $LiTiOPO_4$ were observed in Vendor A. Since secondary phases may increase grain-boundary resistance and disrupt lithium-ion transport pathways, high phase purity is essential for achieving stable electrochemical performance and reliable multilayer processing. Thermal stability was evaluated by TG-DTA analysis [Fig. 1(c)]. Both powders exhibited negligible weight loss throughout the investigated temperature range, indicating suitability for subsequent thermal processing steps such as binder burnout and co-firing. Nevertheless, Vendor B exhibited smoother heat-flow behavior and reduced thermal fluctuations, suggesting superior compositional homogeneity and improved thermal reliability during multilayer ceramic processing. The ionic transport properties of the sintered LATP pellets were quantitatively compared by electrochemical impedance spectroscopy, as shown in Fig. 1(d). The real-axis intercepts of the geometry-normalized impedance spectra corresponded to total room-temperature resistivities of approximately 330 Ω·cm for Vendor A and 200 Ω·cm for Vendor B. Accordingly, the total ionic conductivities calculated using $\sigma = 1/\rho$ were 3.03×10^{-3} S·cm^{-1} for Vendor A and 5.00×10^{-3} S·cm^{-1} for Vendor B, indicating that Vendor B exhibited an approximately 1.65-fold higher ionic conductivity. This result is consistent with the smaller impedance semicircle and lower real-axis intercept observed for Vendor B. The enhanced ionic transport is attributed to its higher NASICON-phase purity and the reduced contributions of resistive secondary phases and grain boundaries. In contrast, the $LiTiOPO_4$ secondary phase detected in Vendor A may partially disrupt continuous lithium-ion transport pathways and increase grain-boundary resistance. Previous studies on surface-mount-technology-compatible multilayer batteries and oxide-based solid-state battery manufacturing have demonstrated that successful multilayer fabrication requires not only electrochemically active materials but also ceramic powders with sufficient phase purity, particle uniformity, processability, and dimensional stability during tape casting, lamination, and co-firing [12–15]. These characteristics strongly influence interfacial integrity, multilayer registration, densification behavior, and electrochemical performance [13–15]. Therefore, LATP powder selection should be considered a critical manufacturing parameter rather than a simple material-screening step. The favorable combination of particle-size uniformity, NASICON-phase purity, thermal stability, and ionic conductivity observed for Vendor B supports its selection for subsequent green-sheet preparation and multilayer ceramic battery fabrication for compact IoT devices, wearable electronics, and AI-enabled edge systems [12,16].

3.2 Optimization of LATP Green Sheet Fabrication

Based on the screening results presented in Section 3.1, Vendor B LATP powder was selected for subsequent multilayer ceramic battery fabrication because of its superior particle uniformity, high phase purity, excellent thermal stability, and lower ionic resistance. Using the selected LATP powder, the green-sheet fabrication process was optimized to establish a robust manufacturing route for multilayer ceramic batteries. The fabrication of defect-free LATP green sheets is essential because sheet quality directly influences printing accuracy, lamination integrity, dimensional stability, and co-firing behavior. In particular, the binder system

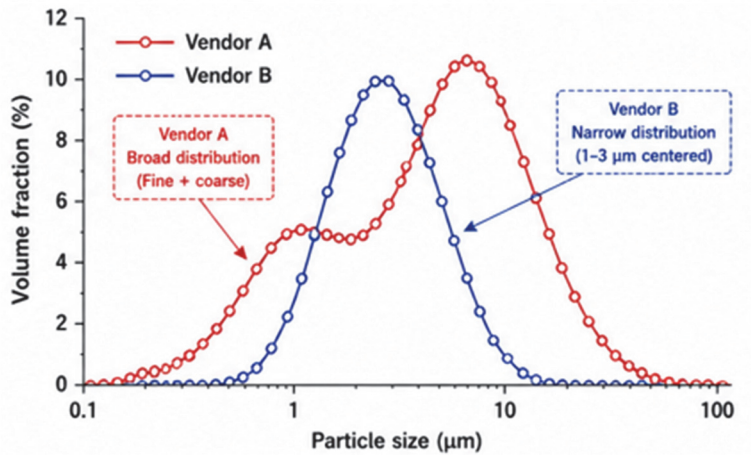

(a)

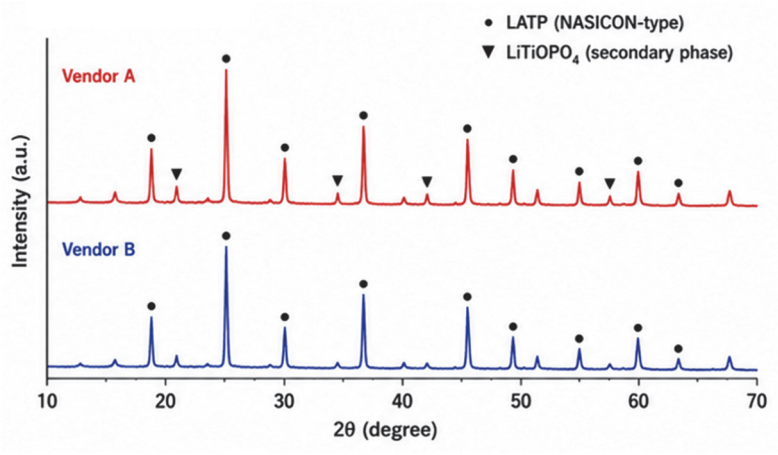

(b)

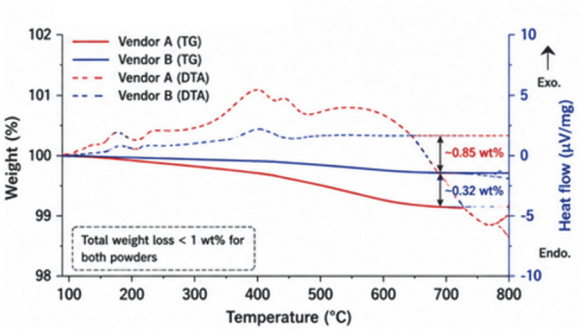

(c)

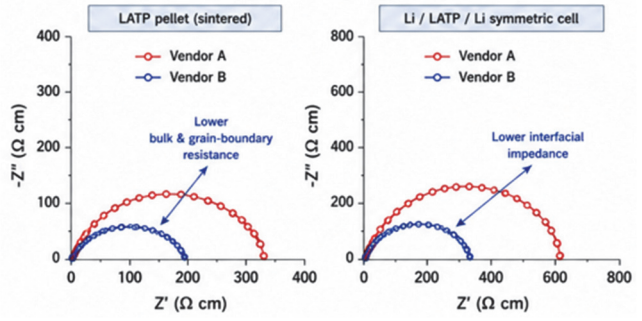

(d)

Fig. 1. Selection of LATP solid electrolytes for multilayer ceramic battery processing: (a) particle size distributions of LATP powders supplied by two vendors, (b) XRD patterns showing differences in phase purity and the presence of secondary phases, (c) TG-DTA analyses comparing the thermal stability of the powders, and (d) Nyquist plots of the sintered LATP pellets (left) and Li/LATP/Li symmetric cells (right)

plays a critical role in determining slurry rheology, particle dispersion, green-sheet flexibility, and mechanical integrity. Similar observations have been reported for oxide-based multilayer solid-state batteries, where slurry characteristics and organic additive content strongly affect tape-casting quality and multilayer process reliability [14,15]. In this study, a mixed polyvinyl butyral (PVB) binder system consisting of BM-2 and BH-3 was employed at a weight ratio of 3:7. BM-2 possesses relatively lower molecular weight and provides improved slurry fluidity and dispersion stability, whereas BH-3 exhibits higher molecular weight and contributes to green-sheet strength and flexibility. Therefore, the combined BM-2/BH-3 system was expected to provide an appropriate balance between processability and mechanical stability during multilayer fabrication. To optimize the organic composition, the total PVB content was systematically varied from 7 to 13 wt%. The dispersant content was fixed at 1 wt% relative to the LATP powder, while ethanol and toluene were used as mixed solvents at a weight ratio of 1:1. The plasticizer content was maintained at 25 wt% of the total binder content. All slurries were prepared by ball milling for 24 h. To minimize the influence of solids loading on rheological behavior, the amount of solvent was adjusted to maintain a solids loading of approximately 45 wt% for all formulations. Figure 2(a) presents the viscosity profiles of LATP slurries containing different total PVB contents. All formulations exhibited typical shear-thinning behavior suitable for tape-casting applications. As the binder content increased, the overall viscosity increased correspondingly. The 7 wt% slurry exhibited relatively low viscosity, indicating insufficient polymer-network formation and limited resistance to particle sedimentation. In contrast, the 13 wt% slurry exhibited excessively high viscosity, particularly in the low-shear region, which may hinder slurry flow and casting uniformity. The 11 wt% slurry exhibited intermediate viscosity and relatively small hysteresis between increasing and decreasing shear cycles, indicating stable dispersion behavior and favorable processability.

The surface morphologies of the LATP green sheets prepared with different PVB contents are compared in Fig. 2(b). Although the differences among the specimens are relatively subtle, systematic comparison reveals clear variations in particle packing, apparent pore distribution, surface heterogeneity, and particle-boundary visibility. The green sheet containing 7 wt% PVB exhibited relatively loose particle packing, irregular interparticle voids, and locally discontinuous particle contacts, indicating insufficient binder content to provide adequate cohesion during tape casting and drying. Increasing the PVB content to 9 wt% improved particle connectivity and reduced the number of large open voids; however, localized agglomeration and nonuniform interparticle spacing remained. Among the investigated compositions, the green sheet containing 11 wt% PVB exhibited the most homogeneous surface morphology. The LATP particles were uniformly distributed, the interparticle spacing was relatively consistent, and large open pores or agglomerated regions were less evident. These observations indicate that 11 wt% PVB provided sufficient particle cohesion while allowing favorable particle rearrangement during casting and drying. In contrast, the 13 wt% specimen exhibited locally smooth regions, partially obscured particle boundaries, and nonuniform surface coverage, suggesting excessive organic accumulation between ceramic particles. Such excessive binder content may restrict particle rearrangement and adversely affect microstructural uniformity. The selection of 11 wt% PVB was based on the combined evaluation of slurry rheology and green-sheet microstructure rather than on visual inspection of the SEM images alone. As shown in Fig. 2(a), the 11 wt% slurry exhibited an intermediate viscosity and relatively small hysteresis between the increasing and decreasing rotational-speed cycles, indicating stable dispersion and suitable flow behavior for tape casting. When considered together with the uniform particle packing, reduced apparent open porosity, and limited surface heterogeneity observed in Fig. 2(b), these results demonstrate that the 11 wt% PVB formulation provided the most favorable balance among slurry processability, green-sheet cohesion, microstructural uniformity, and mechanical integrity. Similar behavior has been reported for lithium borosilicate and oxide-based solid-electrolyte sheets, in which insufficient binder content resulted in poor sheet integrity, whereas excessive binder content deteriorated microstructural homogeneity [14,15]. Therefore, the 11 wt% PVB formulation based on the BM-2/BH-3 ratio of 3:7 was selected for subsequent electrode printing, lamination, co-firing, and electrochemical evaluation.

3.3 Suppression of Printing-Induced Warping through Drying Optimization

Following optimization of the LATP green-sheet composition, multilayer electrode fabrication was investigated through sequential printing, lamination, and warm isostatic pressing (WIP). Unlike conventional multilayer ceramic capacitor processing, MLCB fabrication requires repeated deposition of electro-chemically active materials and metallic current collectors onto LATP electrolyte sheets. Differences in solvent evaporation, drying shrinkage, and thermal expansion among these layers can therefore cause dimensional instability during multilayer processing.

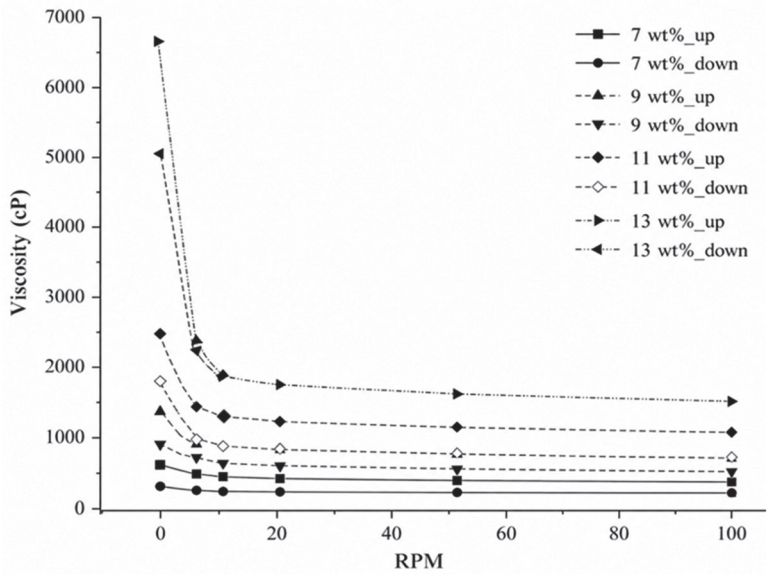

(a)

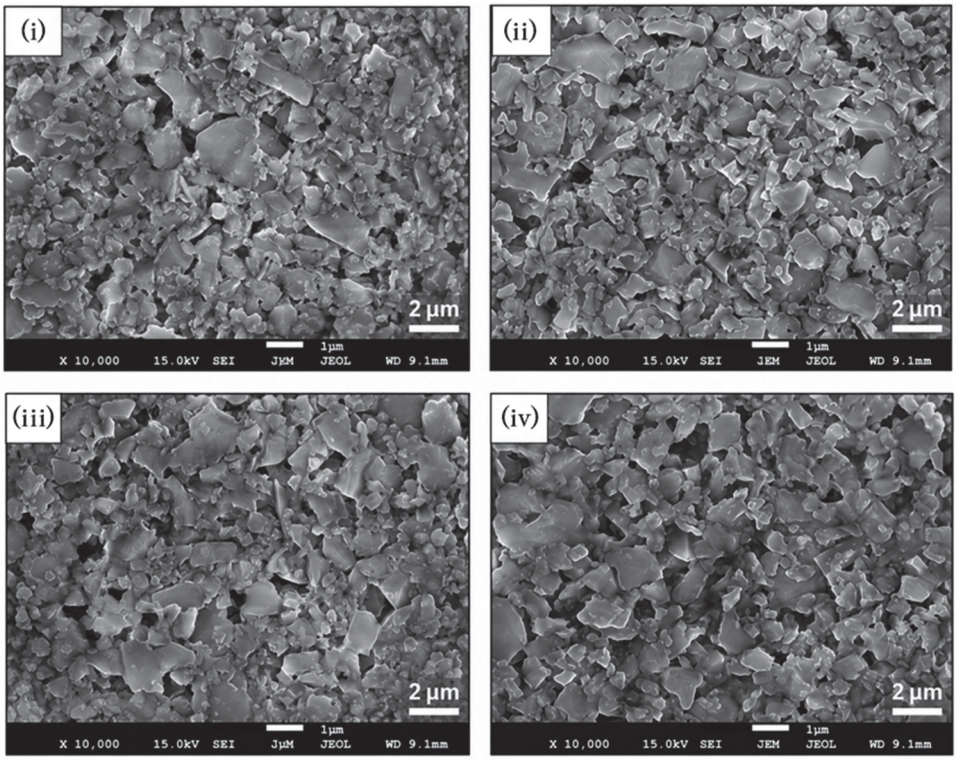

(b)

Fig. 2. Optimization of Vendor B LATP green sheet fabrication through PVB binder control: (a) viscosity profiles of Vendor B LATP slurries containing 7−13 wt% PVB measured during increasing (up) and decreasing (down) rotational speed cycles and (b) top-view FE-SEM images of LATP green sheets prepared with PVB contents of (i) 7 wt%, (ii) 9 wt%, (iii) 11 wt%, and (iv) 13 wt%

The optimized LATP green sheets were slit into 6-inch bar-type sheets with an effective width of 160 mm to minimize edge-related variations. Three alignment holes were punched into each sheet and used as registration references during printing and stacking. As illustrated in Fig. 3(a), an LVP-based cathode paste and a Cu powder-based current-collector paste were sequentially printed onto the LATP sheets. The printing sequence consisted of first cathode printing, Cu current-collector printing, and second cathode overprinting. Two-stage hot-air drying was applied after each printing step to immobilize the patterns and maintain dimensional accuracy. Repeated deposition of active-material and metallic pastes can induce differential drying shrinkage, solvent redistribution, and residual-stress accumulation in multilayer structures [17–19]. These effects are particularly relevant to MLCBs because the LVP, Cu, and LATP layers have different organic formulations and drying characteristics. Under the initial drying condition of 75°C followed by 85°C, considerable sheet warping developed after repeated printing. Rapid solvent evaporation and thermal gradients between the printed layers and LATP substrate generated residual stresses, reducing sheet flatness and electrode-registration accuracy and occasionally causing misalignment during stacking. To suppress this deformation, the first- and second-stage drying temperatures were reduced to 65 and 75°C, respectively. The lower-temperature profile reduced the

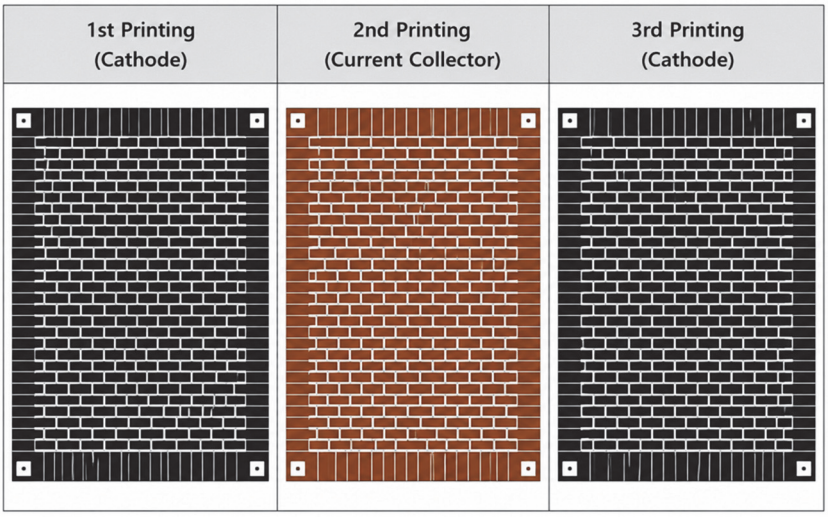

(a)

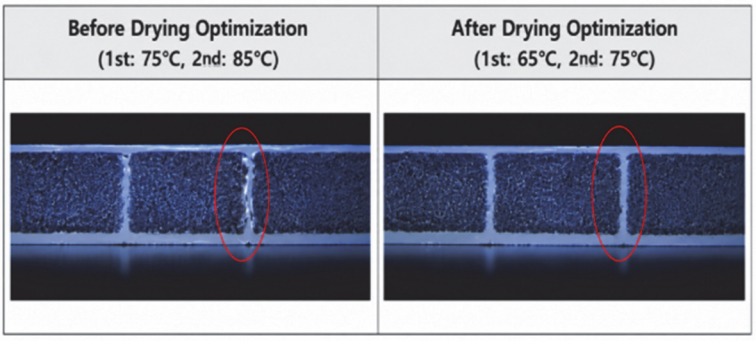

(b)

Fig. 3. Suppression of printing-induced warping through drying optimization: (a) sequential electrode-printing process consisting of first cathode printing, current collector printing, and second cathode printing on the LATP green sheets and (b) cross-sectional optical microscopy images of WIP-treated laminated bars fabricated under conventional drying conditions (1st: 75°C, 2nd: 85°C) and optimized drying conditions (1st: 65°C, 2nd: 75°C), illustrating the influence of drying temperature on electrode alignment and multilayer stacking precision

solvent evaporation rate and thermal gradients, thereby limiting stress accumulation within the LATP sheets. Consequently, no apparent warping was observed after the three consecutive printing steps, and the dimensional stability of the printed sheets was substantially improved. The printed sheets were subsequently stacked and consolidated by WIP. Because the laminated body contained repeated LVP electrode and Cu current-collector layers, the lamination conditions were optimized to improve interfacial contact without damaging the printed patterns. WIP was performed at approximately 80°C and 1,400 kgf cm^{-2} for 10 min after a 10 min preheating step. No visible layer separation or interfacial delamination was observed after treatment, indicating effective consolidation of the multilayer structure. Figure 3(b) compares cross-sectional optical microscopy images of WIP-treated laminated bars prepared using the initial and optimized drying profiles. The specimen dried at 75/85°C exhibited noticeable electrode displacement and nonuniform layer spacing owing to sheet warping. In contrast, the specimen processed at 65/75°C showed improved dimensional stability and multilayer registration, with relatively parallel electrode layers and more uniform spacing between adjacent layers. These results demonstrate that sequential printing of LVP cathodes and Cu current collectors introduces drying-related dimensional challenges in MLCB fabrication. Careful control of drying and lamination conditions is therefore essential for maintaining sheet flatness, electrode alignment, and multilayer structural integrity. The optimized 65/75°C drying profile combined with WIP consolidation provides a practical processing strategy for adapting multilayer ceramic manufacturing technologies to oxide-based battery fabrication.

3.4 Optimization of Binder Burnout and Co-firing Behavior of MLCBs

To establish a co-firing process that minimizes defects in multilayer ceramic batteries (MLCBs), the thermal decomposition behavior of the constituent materials was systematically investigated using thermogravimetric and differential thermal analyses (TG–DTA). Measurements were performed on the LVP cathode paste, LATP green sheet, Cu current-collector paste, and assembled laminated green chip to determine suitable debinding and co-firing conditions. Figure 4 presents the corresponding TG–DTA profiles. The LVP cathode paste exhibited rapid weight loss between approximately 200 and 350°C, corresponding to the decomposition of organic binders and processing additives, while minor weight loss below 200°C was attributed to residual solvent evaporation. The LATP green sheet showed more gradual decomposition extending to higher temperatures, indicating that some binder components remained stable over an intermediate temperature range. Among the investigated materials, the Cu current-collector paste exhibited the broadest decomposition range, extending from approximately 200 to 450°C, owing to its complex organic formulation for printability, adhesion, and particle dispersion. Consequently, the laminated green chip exhibited overlapping decomposition events originating from the LATP sheet, LVP cathode, and Cu current-collector layers. Most organic decomposition occurred between 200 and 450°C, indicating that simultaneous gas evolution from multiple layers is a critical issue during binder burnout. The thermal decomposition process was therefore divided into three stages: (i) solvent evaporation below 200°C, (ii) primary organic decomposition between 200 and 450°C, and (iii) residual organic removal and structural stabilization above approximately 450°C. Because intensive decomposition of the cathode and current-collector pastes occurred mainly between 200 and 350°C, slow heating and sufficient holding times were considered necessary to suppress rapid gas evolution and internal pressure buildup. The use of Cu as the internal current collector introduced an additional processing constraint. Unlike noble metals such as Ag or Pt, Cu is readily oxidized at elevated temperatures and therefore requires a controlled reducing atmosphere. Accordingly, the thermal schedule had to simultaneously ensure sufficient binder removal, preservation of metallic Cu, and densification of the ceramic layers without severe structural degradation. Rapid binder decomposition in multilayer ceramic structures can generate excessive internal pressure, leading to blistering, delamination, and reduced process yield, particularly when gas-escape pathways are limited [20,21]. In addition, controlled thermal profiles and reduced firing temperatures can decrease thermal mismatch, suppress interfacial reactions, and improve dimensional stability [22,23]. Based on these considerations, an optimized two-step debinding and co-firing process was established, as summarized in Fig. 5. The first debinding step was conducted at 350°C under N_2 with a heating rate of 0.3°C min^{-1} to promote gradual removal of organic species. The second step was performed at 650°C under N_2 + 1% H_2 with a heating rate of 1°C min^{-1} to remove residual organics and maintain the Cu current collector under a mildly reducing atmosphere. Finally, co-firing was carried out at 850°C under N_2 + 1% H_2 with a heating rate of 1°C min^{-1} and a holding time of 2 h. The co-firing temperature was selected by considering the densification behavior of the phosphate-based ceramic components and the stability of the multilayer structure under reducing conditions. Figure 6 presents low- and high-magnification cross-sectional SEM images

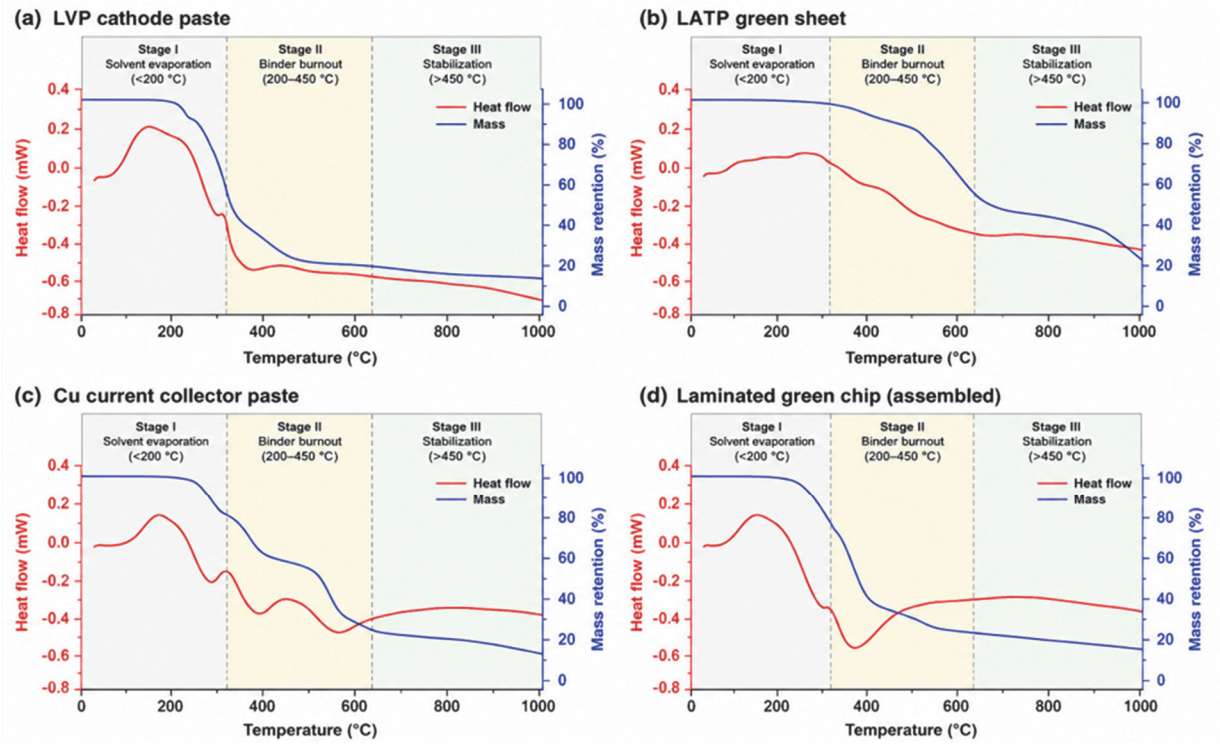

Fig. 4. TG-DTA profiles of the constituent materials used for multilayer ceramic battery fabrication: (a) LVP cathode paste, (b) LATP green sheet, (c) Cu current collector paste, and (d) laminated green chip

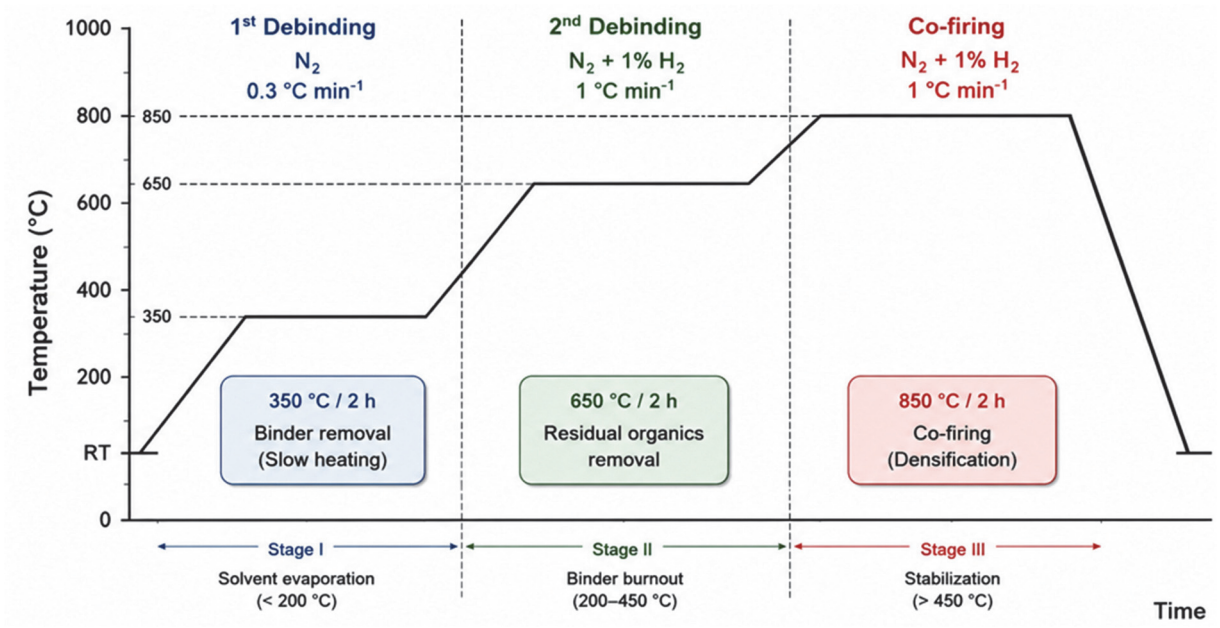

Fig. 5. Optimized two-step debinding and co-firing schedule for MLCC-compatible MLCBs

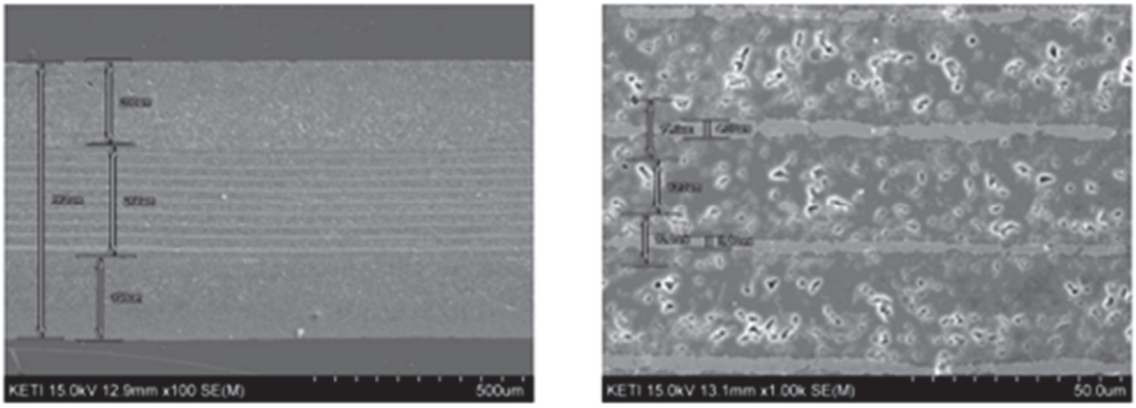

Fig. 6. Cross-sectional SEM images of the co-fired multilayer ceramic battery

of the MLCB fabricated using the optimized thermal schedule. The co-fired specimen retained the overall multilayer architecture without macroscopic blistering, delamination, severe interfacial cracking, or catastrophic layer distortion. The active-electrode layers were less than approximately 5 μm thick and were positioned between the LATP electrolyte layers together with the Cu current-collector layers. Because of the small thickness of the active-electrode layers, the low-magnification image required to visualize the entire multilayer structure did not provide sufficient spatial resolution for reliable quantitative measurement of each individual layer. Conversely, high-magnification images capable of resolving the sub-5-μm layers covered only limited local regions and could not represent the thickness uniformity of the entire device. Therefore, uncertain quantitative values for the individual electrode-layer thicknesses were not derived from the present SEM images. Nevertheless, the cross-sectional observations confirmed that the layered configuration was generally preserved after lamination, debinding, and co-firing. The electrode and current-collector layers remained distinguishable and relatively continuous within the spatial resolution of SEM, and no extensive separation was observed at the interfaces with the LATP electrolyte. These observations indicate structural compatibility among the constituent layers under the applied co-firing conditions. It should be emphasized, however, that the present SEM observations demonstrate morphological continuity rather than complete chemical compatibility among LATP, LVP, and Cu. Elemental mapping and high-resolution interfacial analyses were not performed in the present study. Further investigations using SEM–EDS mapping, elemental line scanning, and transmission electron microscopy will be required to evaluate possible elemental interdiffusion, local reaction-layer formation, and nanoscale interfacial degradation.

3.5 Demonstration of a Functional Multilayer Ceramic Battery

To verify whether the co-fired multilayer structure retained electrochemical functionality, charge–discharge measurements were performed on the sintered MLCB chips at room temperature at 0.01 C within a voltage window of 0.0–1.3 V. Figure 7 presents the voltage–capacity profiles of the prototype device. The co-fired MLCB exhibited distinguishable charge and discharge behavior without electrical short-circuiting or catastrophic voltage failure, indicating that lithium-ion transport and electrochemical reactions were retained after tape casting, printing, lamination, debinding, and co-firing. The prototype delivered a discharge capacity of approximately 2.5–2.7 μAh and a charge capacity of approximately 3.0 μAh, corresponding to an estimated initial Coulombic efficiency of 83–90%. A pronounced voltage hysteresis between the charge and discharge curves indicated substantial internal polarization associated with the LATP electrolyte, electrode/electrolyte interfaces, and current-collection pathways. Therefore, the present electrochemical performance remains insufficient for practical applications. The primary objective of this study was not to demonstrate optimized battery performance, but to establish the feasibility of integrating oxide-based battery materials into an MLCC-compatible multilayer ceramic manufacturing process. Accordingly, the charge–discharge results should be interpreted as evidence that basic electrochemical functionality was preserved after the complete fabrication and co-firing processes. The

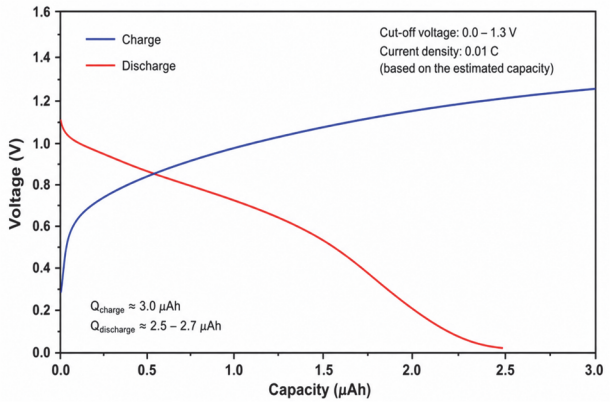

Fig. 7. Charge–discharge profiles of the co-fired multilayer ceramic battery measured at room temperature under a current density of 0.01 C within a voltage window of 0.0–1.3 V

fabricated device represents an initial process-feasibility prototype rather than an electrochemically optimized battery. Further improvement will require optimization of the LVP electrode, Cu current collector, LATP solid-electrolyte layer, and electrode/electrolyte interfaces. Full-cell electrochemical impedance spectroscopy, rate-capability measurements, and long-term cycling tests will also be necessary to identify the dominant resistance and degradation mechanisms and to improve reversible capacity, Coulombic efficiency, and cycling stability. Overall, these results provide a manufacturing foundation for the future development of oxide-based multilayer ceramic batteries.

4 Conclusions

In this study, an MLC-compatible manufacturing platform for oxide-based multilayer ceramic batteries (MLCBs) was successfully developed using LATP solid electrolytes, LVP cathodes, and Cu current collectors. Conventional multilayer ceramic processes, including tape casting, screen printing, lamination, debinding, and co-firing, were successfully adapted for MLCB fabrication. Among the commercial LATP powders evaluated, Vendor B was selected because of its superior phase purity, particle-size uniformity, thermal stability, and ionic conductivity. An optimized green-sheet formulation containing 11 wt% PVB binder (BM-2/BH-3 = 3:7) provided excellent slurry stability and microstructural uniformity. Drying-induced warpage generated during repeated printing of LVP cathodes and Cu current collectors was effectively suppressed through optimization of drying and lamination conditions. TG–DTA-guided thermal analysis enabled the design of an optimized two-step debinding and co-firing process. By controlling organic removal under a Cu-compatible reducing atmosphere, defect-free multilayer structures were obtained without significant blistering, delamination, or interfacial defects. Cross-sectional SEM observations confirmed continuous interfaces and uniform densification throughout the co-fired structure. Charge–discharge measurements verified that electrochemical functionality was retained after the complete manufacturing process. Although the prototype device exhibited limited capacity and noticeable voltage hysteresis, stable charge–discharge behavior confirmed the feasibility of integrating oxide-based battery materials into a multilayer ceramic manufacturing platform. Overall, this work establishes a practical manufacturing foundation for oxide-based MLCBs and demonstrates the potential of adapting mature multilayer ceramic technologies to all-solid-state battery fabrication. Future studies should focus on improving electrochemical performance through optimization of electrode composition, electrolyte densification, interfacial engineering, and multilayer architecture.

ORCID

Jung Rag Yoon https://orcid.org/0000-0002-9206-8701

Acknowledgement

This work was supported by the Technology Innovation Program (RS-2024-00430833, Development of MLCC commercialization technology for automotive electronics an alternative to rare earth for high reliability response) funded by the Ministry of Trade, Industry & Energy (MOTIE, Korea).

Conflict of Interest

The author (Jung Rag Yoon) currently serves on the editorial board of JEEM, but was not involved in any part of the publication process. Other than this, the authors declare that they have no relevant potential conflicts of interest.

Author Contributions

Won-Su Lee: Investigation, Formal analysis, Data Curation, Writing – Original Draft.
Jong Kyu Lee: Methodology, Validation, Resources.
Jung Rag Yoon: Conceptualization, Supervision, Writing – Review & Editing, Project administration, Funding acquisition.

Data Availability

Data openly available in a public repository that issues datasets with DOIs.

References

[1] R. H. Lee, D. W. Lee, J. K. Lee, K. N. Kim, J. R. Yoon, and S. H. Lee, *J. Energy Storage*, **77**, 110018 (2024).
doi: https://doi.org/10.1016/j.est.2023.110018
[2] R. H. Lee, S. J. Jo, J. K. Lee, J. R. Yoon, H. K. Kim, and S. H. Lee, *ACS Appl. Energy Mater.*, **6**, 2812 (2023).
doi: https://doi.org/10.1021/acsaem.2c03706
[3] R. H. Lee, C. Y. Kang, J. K. Lee, B. S. Jin, K. N. Kim, H. S. Kim, J. R. Yoon, and S. H. Lee, *NPG Asia Mater.*, **16**, 42 (2024).
doi: https://doi.org/10.1038/s41427-024-00563-7
[4] J. H. Yin, H. Zhu, S. J. Yu, Y. B. Dong, Q. Y. Wei, G. Q. Xu, Y. Xiong, and Y. Qian, *Adv. Eng. Mater.*, **25**, 2300566 (2023).
doi: https://doi.org/10.1002/adem.202300566
[5] C. Luo, M. Yi, Z. Cao, W. Hui, and Y. Wang, *ACS Appl. Electron. Mater.*, **6**, 641 (2024).
doi: https://doi.org/10.1021/acsaelm.3c01747
[6] M. Monchak, T. Hupfer, A. Senyshyn, H. Boysen, D. Chernyshov, T. Hansen, K. G. Schell, E. C. Bucharsky, M. J. Hoffmann, and H. Ehrenberg, *Inorg. Chem.*, **55**, 2941 (2016).
doi: https://doi.org/10.1021/acs.inorgchem.5b02821
[7] K. Hiraoka, Y. Sato, S. Seki, and K. Yamamoto, *ACS Appl. Energy Mater.*, **9**, 818 (2026).
doi: https://doi.org/10.1021/acsaem.5c03001
[8] Y. W. Yoo, H. S. Oh, J. K. Lee, J. R. Yoon, and S. H. Lee, *Energy Mater. Adv.*, **5**, 0147 (2024).
doi: https://doi.org/10.34133/energymatadv.0147
[9] D. Wang, Q. Yan, M. Li, H. Gao, J. Tian, Z. Shan, N. Wang, J. Luo, M. Zhou, and Z. Chen, *Nanoscale*, **13**, 2811 (2021).
doi: https://doi.org/10.1039/d0nr08305d
[10] T. Fabre, M. Lachal, H. Raj, V. Pralong, R. Bouchet, and M. C. Steil, *J. Eur. Ceram. Soc.*, **45**, 116941 (2025).
doi: https://doi.org/10.1016/j.jeurceramsoc.2024.116941
[11] S. H. Kim, Y. C. Hwang, S. H. Kang, S. Y. Park, S. M. Koo, and W. H. Shin, *J. Korean Inst. Electr. Electron. Mater. Eng.*, **39**, 210 (2026).
doi: https://doi.org/10.4313/JEEM.2026.39.2.11
[12] R. H. Lee, C. Y. Kang, W. J. Jeon, J. K. Lee, H. N. Jo, X. Y. Jin, S. J. Kim, J. R. Yoon, and S. H. Lee, *Materials Today*, **93**, 103209 (2026).
doi: https://doi.org/10.1016/j.mattod.2026.103209
[13] W. Ahn, *J. Korean Inst. Electr. Electron. Mater. Eng.*, **38**, 521 (2025).
doi: https://doi.org/10.4313/JEEM.2025.38.5.7
[14] Y. Jo, Y. Choi, H. Shin, M. Choi, D. Yeo, and Y. Heo, *J. Non-Cryst. Solids*, **654**, 123443 (2025).
doi: https://doi.org/10.1016/j.jnoncrysol.2025.123443
[15] J. Park, J. Choi, J. Seo, W. Nam, S. Lee, S. Cho, K. Park, G. An, B. Park, and M. Choi, *Micromachines*, **16**, 39 (2025).
doi: https://doi.org/10.3390/mi16010039
[16] J. R. Yoon, S. N. Seo, M. W. Ha, and M. T. Cho, *J. Korean Inst. Electr. Electron. Mater. Eng.*, **39**, 34 (2026).
doi: https://doi.org/10.4313/JEEM.2026.39.1.5
[17] T. Nakamura, T. Kakibe, and S. Takahashi, *Solid State Ionics*, **417**, 116685 (2024).
doi: https://doi.org/10.1016/j.ssi.2024.116685
[18] N. Fonseca, S. V. Thummalapalli, S. Jambhulkar, D. Ravichandran, Y. Zhu, D. Patil, V. Thippanna, A. Ramanathan, W. Xu, S. Guo, H. Ko, M. Fagade, A. M. Kannan, Q. Nian, A. Asadi, G. Miquelard-Garnier, A. Dmochowska, M. K. Hassan, M. Al-Ejji, H. M. El-Dessouky, F. Stan, and K. Song, *Small*, **19**, 2302718 (2023).
doi: https://doi.org/10.1002/smll.202302718
[19] J. M. Lee, D. S. Cheong, S. H. Kang, T. R. Acharya, E. H. Choi, and W. H. Shin, *J. Korean Inst. Electr. Electron. Mater. Eng.*, **37**, 445 (2024).
doi: https://doi.org/10.4313/JKEM.2024.37.4.13
[20] A. Sazvar, M. Hajibandeh, P. Vafaei, E. Hosseinzadeh, and M. Jabbari, *J. Energy Storage*, **101**, 113863 (2024).
doi: https://doi.org/10.1016/j.est.2024.113863
[21] X. Han, S. Wang, Y. Xu, G. Zhong, Y. Zhou, B. Liu, X. Jiang, X. Wang, Y. Li, Z. Zhang, S. Chen, C. Wang, Y. Yang, W. Zhang, J. Wang, J. Liu, and J. Yang, *Energy Environ. Sci.*, **14**, 5044 (2021).
doi: https://doi.org/10.1039/d1ee01494c
[22] K. Rajeswari, S. Chaitanya, P. Biswas, M. B. Suresh, Y. S. Rao, and R. Johnson, *J. Ceram. Process. Res.*, **16**, 24 (2015).
doi: https://doi.org/10.36410/jcpr.2015.16.1.24
[23] X. Kuang, G. Carotenuto, and L. Nicolais, *Adv. Perform. Mater.*, **4**, 257 (1997).
doi: https://doi.org/10.1023/A:1008621020555